

RESEARCH LETTER

10.1002/2015GL065227

Key Points:

- A robust methodology is proposed to investigate the mechanical behavior of snow from 3-D images
- The full effective elastic stiffness tensor of snow was computed for 31 tomographic images
- The influence of density and microstructure (metamorphism, anisotropy, etc.) of snow are highlighted

Supporting Information:

- Text S1

Correspondence to:

A. Wautier,
antoine.wautier@gmail.com

Citation:

Wautier, A., C. Geindreau, and F. Flin (2015), Linking snow microstructure to its macroscopic elastic stiffness tensor: A numerical homogenization method and its application to 3-D images from X-ray tomography, *Geophys. Res. Lett.*, 42, 8031–8041, doi:10.1002/2015GL065227.

Received 16 JUL 2015

Accepted 2 SEP 2015

Accepted article online 7 SEP 2015

Published online 3 OCT 2015

Linking snow microstructure to its macroscopic elastic stiffness tensor: A numerical homogenization method and its application to 3-D images from X-ray tomography

A. Wautier^{1,2,3}, C. Geindreau^{2,3}, and F. Flin¹
¹Météo-France - CNRS, CNRM - GAME UMR 3589, CEN, Saint-Martin-d'Hères, France, ²Université Grenoble Alpes, 3SR, Grenoble, France, ³CNRS, 3SR, Grenoble, France

Abstract The full 3-D macroscopic mechanical behavior of snow is investigated by solving kinematically uniform boundary condition problems derived from homogenization theories over 3-D images obtained by X-ray tomography. Snow is modeled as a porous cohesive material, and its mechanical stiffness tensor is computed within the framework of the elastic behavior of ice. The size of the optimal representative elementary volume, expressed in terms of correlation lengths, is determined through a convergence analysis of the computed effective properties. A wide range of snow densities is explored, and power laws with high regression coefficients are proposed to link the Young's and shear moduli of snow to its density. The degree of anisotropy of these properties is quantified, and Poisson's ratios are also provided. Finally, the influence of the main types of metamorphism (isothermal, temperature gradient, and wet snow metamorphism) on the elastic properties of snow and on their anisotropy is reported.

1. Introduction

Snow is a highly porous material that exists close to its melting point and exhibits a complex microstructure constantly evolving over time. Because overall mechanical properties of snow are strongly influenced by its density [Mellor, 1975] and the topology of its microstructure [Shapiro *et al.*, 1997], a correct multiscale modeling of the mechanical properties of snow is of great interest when it comes to avalanche risk forecasting. In particular, elastic properties of snow layers are known to play a significant role in slab release processes [see, e.g., Schweizer and Camponovo, 2002; Heierli *et al.*, 2008; Gaume *et al.*, 2015] but are difficult to measure experimentally with accuracy [see, e.g., Mellor, 1975; Schweizer and Camponovo, 2002; Hagenmuller *et al.*, 2014; Köchle and Schneebeli, 2014].

Application of X-ray tomography to snow [e.g., Brzoska *et al.*, 1999; Schneebeli, 2004; Kämpfer *et al.*, 2005; Flin and Brzoska, 2008; Chen and Baker, 2010; Srivastava *et al.*, 2010; Pinzer *et al.*, 2012; Adams and Walters, 2014; Calonne *et al.*, 2015] has allowed its complex microscale geometry to be described. Nowadays, good databases of 3-D images for the different snow types described in the international classification [Fierz *et al.*, 2009] are available [e.g., Calonne *et al.*, 2012; Löwe *et al.*, 2013].

Given a precise description of the ice skeleton of snow, its complex behavior can be determined from the fairly well established physical and mechanical properties of ice [Schulson and Duval, 2009]. From this point, the macroscopic behavior of snow considered as a homogeneous material can be upscaled using techniques derived from the homogenization theory based on the assumption of the separation of scales [Dormieux and Bourgeois, 2002; Auriault *et al.*, 2010]. In our case, such an assumption is valid when the microscopic length scale is much smaller than the characteristic length over which the macroscopic loading varies in space. In recent works, a combination of X-ray tomography imaging, finite element techniques, and ever increasing computing power has been used to bridge the gap between the topology of the ice skeleton of snow and its mechanical behavior [Pieritz *et al.*, 2004; Schneebeli, 2004; Srivastava *et al.*, 2010; Hagenmuller *et al.*, 2014; Chandel *et al.*, 2014; Köchle and Schneebeli, 2014; Schleef *et al.*, 2014]. However, while Srivastava *et al.* [2010] used an approach rigorously based on the homogenization theory [Van Rietbergen *et al.*, 1996], most of the upscaled snow properties found in the literature have been obtained thanks to numerical simulations of

“real” unidirectional experiments assuming an isotropic macroscopic behavior [e.g., Hagenmuller et al., 2014; Köchle and Schneebeli, 2014].

Following the study of Calonne et al. [2011, 2012, 2014a, 2014b] on the homogenization of the heat and mass transport properties of snow, the aim of this paper is to propose a rigorous multiscale modeling of the elastic stiffness tensor of snow and to calculate the relative influence of the density and the topology of the microstructure on its macroscopic properties. Quantitative results are given for a very wide range of densities (from 103 to 544 kg m⁻³), and the influence of the main types of metamorphism is investigated.

2. Numerical Homogenization Procedure for Kinematically Uniform Boundary Conditions

Boundary value problems derived from homogenization theories were solved numerically on 3-D snow images obtained by microtomography. The representative elementary volume (REV) required to deduce the macroscopic mechanical properties of the sample varies with the choice of boundary conditions. Three types of boundary condition described in homogenization theories are considered to give relatively small REV. In decreasing order of REV [Kanit et al., 2003], these are statically uniform boundary conditions (SUBC), with a macroscopic homogenous stress imposed on the boundary, kinematically uniform boundary conditions (KUBC), with a macroscopic homogenous strain imposed on the boundary, and periodic boundary conditions (PBC). The periodic boundary conditions arise from enforcing the periodicity of the displacement field over the three directions of space and the periodicity of the normal stress across the sample boundaries. Although these are considered to give the best convergence with respect to the size of the REV [Kanit et al., 2003], their application to a nonperiodic microstructure is not straightforward. It is necessary, for example, to enclose the sample by a virtual boundary or assume that the pores are filled by a soft material. In order to avoid the introduction of such artifacts, KU boundary conditions were chosen.

The numerical homogenization procedure used is composed of the following four steps that are summarized in Figure 1.

2.1. Converting Images Into 3-D Meshes (Step 1)

Using the MATLAB open-source toolbox *iso2mesh* [Fang and Boas, 2009], a tetrahedral mesh was fitted to each original 3-D binary image of typical size 600³ voxels. The toolbox was used with the meshing option *cgalmesh*, and adaptative meshes of controlled density and quality were created from binary snow images. The resulting meshes were composed of a typical number of 2 million elements (Figure 1).

2.2. Boundary Value Problem Definition in Abaqus (Step 2)

Assuming separation of scales, it is possible to deduce macroproperties of a given material by performing numerical tests on a REV. Using Hill's lemma [Hill, 1963], the macroscopic stress tensor Σ and the macroscopic homogeneous strain tensor \mathbf{E} are deduced from their microscopic counterparts (σ and ϵ) by computing their mean values over the REV (V):

$$\mathbf{E} = \langle \epsilon \rangle = \frac{1}{|V|} \int_V \epsilon \, dV \quad \text{and} \quad \Sigma = \langle \sigma \rangle = \frac{1}{|V|} \int_V \sigma \, dV$$

Because of Green's formula, the mean stress and strain can either be averaged over the sample's volume or its boundary. For instance, if ϵ is kinematically admissible to a continuous displacement field $\mathbf{u}(\mathbf{x})$, the equivalent strain tensor can be computed with the equivalent formula

$$\mathbf{E} = \frac{1}{|V|} \int_{\partial V} \mathbf{u} \otimes_s \mathbf{n} \, dS$$

where \otimes_s is the symmetrized tensorial product and \mathbf{n} the outward normal vector on the boundary ∂V . Given this localization property, an informed choice of boundary conditions allows control of the macrostress or strain that is imposed on a given sample and indirectly of the size of the REV. We applied the KUBC approach and practically implemented it thanks to the use of the plug-in *HomTools* [Lejeunes et al., 2011] developed for the commercial finite element software Abaqus. This plug-in enables the automatic definition of the linear relationship on ∂V between the displacements \mathbf{u} and the macroscopic homogeneous strain \mathbf{E} defined as $\mathbf{u} = \mathbf{E} \cdot \mathbf{x}$ for $\mathbf{x} \in \partial V$ (Figure 1).

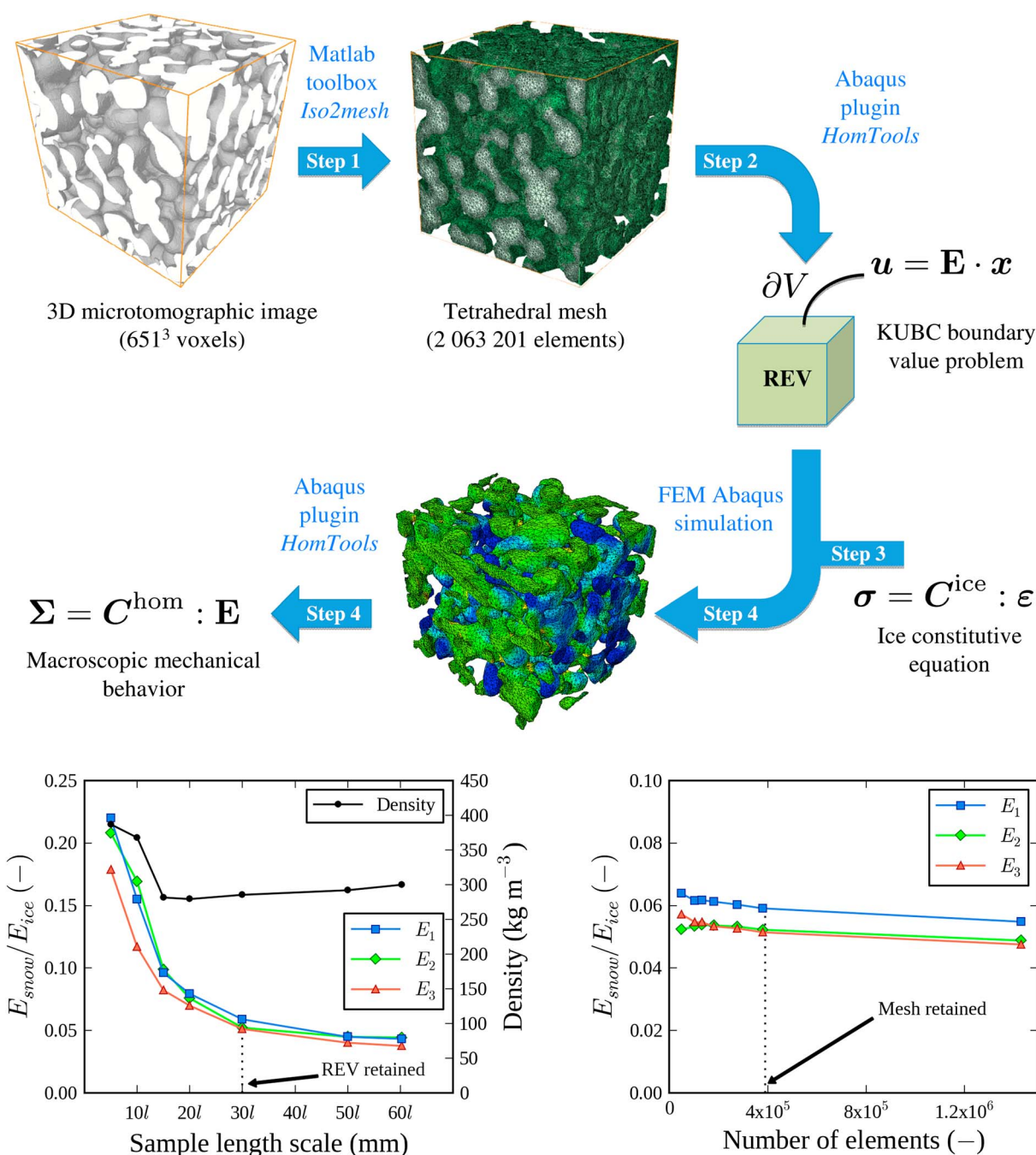


Figure 1. (top) Four-step procedure used in order to transform 3-D microtomograph images of snow into finite element models and numerically solve KUBC homogenization boundary value problems. (bottom) Convergence analysis of the Young's modulus with respect to the dimensionless size of the sample and the size of the mesh used. Concerning the volume convergence analysis, the density curve is also plotted.

2.3. Ice Constitutive Equation (Step 3)

The polycrystalline ice skeleton is considered as a homogeneous isotropic elastic material with stiffness tensor C^{ice} defined by

$$\sigma = C^{ice} : \epsilon = \frac{E}{1 + \nu} \left(\epsilon + \frac{\nu}{1 - 2\nu} \text{Tr}(\epsilon) \mathbf{1} \right)$$

where the symbol $:$ indicates the double contraction operator, E and ν are the Young's modulus and the Poisson's ratio, respectively, and $\mathbf{1}$ is the second-order identity tensor. E is known to range from 0.2 GPa to

9.5 GPa [Chandel *et al.*, 2014]. In order to exclude the effect of variation in E from the discussion, all results in this paper are normalized by setting E equal to 1. Based on the literature, Poisson's ratio ν is chosen equal to 0.3.

2.4. Computing the Homogenized Stiffness Tensor (Step 4)

The homogenization problem to be solved on the REV (V) is written

$$\begin{cases} \operatorname{div} \boldsymbol{\sigma} = 0 & \text{for } \mathbf{x} \in V \\ \mathbf{u} = \mathbf{E} \cdot \mathbf{x} & \text{for } \mathbf{x} \in \partial V \\ \boldsymbol{\epsilon} = \frac{1}{2} (\nabla \mathbf{u} + (\nabla \mathbf{u})^T) & \text{for } \mathbf{x} \in V \\ \boldsymbol{\sigma} = \mathbf{C}(\mathbf{x}) : \boldsymbol{\epsilon} & \text{for } \mathbf{x} \in V \end{cases} \quad (1)$$

where $\mathbf{C}(\mathbf{x})$ is the local stiffness tensor equal to $\mathbf{0}$ in the air phase and \mathbf{C}^{ice} in the ice phase.

With the knowledge of the microscopic stress, its homogenized macroscopic counterpart can be computed, and the linear relationship between $\boldsymbol{\Sigma}$ and \mathbf{E} gives the homogenized stiffness tensor \mathbf{C}^{hom} as follows:

$$\boldsymbol{\Sigma} = \frac{1}{|V|} \int_V \boldsymbol{\sigma} \, dV = \mathbf{C}^{\text{hom}} : \mathbf{E}$$

The homogenized stiffness tensor \mathbf{C}^{hom} exhibits only 21 independent components in the most general case. By setting five out of six of the independent components of \mathbf{E} equal to 0 ($\mathbf{E} = \delta_{ij} \mathbf{e}_i \otimes \mathbf{e}_j$ where δ_{ij} is the Kronecker delta), only six numerical simulations are needed in order to fully compute \mathbf{C}^{hom} . Based on the features of the stiffness matrices computed on all the 3-D images, it appears reasonable to model snow as an orthotropic material (i.e., a material with two perpendicular planes of symmetry) with principal axes ($\mathbf{e}_1, \mathbf{e}_2, \mathbf{e}_3$), \mathbf{e}_3 being along the direction of gravity. By doing so, the macroscopic behavior is described thanks to three Young's moduli, three shear moduli, and six Poisson's ratios. The orthotropic behavior stays general enough to capture anisotropic behaviors. The inverse of \mathbf{C}^{hom} , i.e., the compliance matrix, is written

$$\begin{pmatrix} E_{11} \\ E_{22} \\ E_{33} \\ 2E_{23} \\ 2E_{13} \\ 2E_{12} \end{pmatrix} = \begin{pmatrix} 1/E_1 & -\nu_{12}/E_1 & -\nu_{13}/E_1 & 0 & 0 & 0 \\ -\nu_{21}/E_2 & 1/E_2 & -\nu_{23}/E_2 & 0 & 0 & 0 \\ -\nu_{31}/E_3 & -\nu_{32}/E_3 & 1/E_3 & 0 & 0 & 0 \\ 0 & 0 & 0 & 1/G_{23} & 0 & 0 \\ 0 & 0 & 0 & 0 & 1/G_{13} & 0 \\ 0 & 0 & 0 & 0 & 0 & 1/G_{12} \end{pmatrix} \cdot \begin{pmatrix} \Sigma_{11} \\ \Sigma_{22} \\ \Sigma_{33} \\ \Sigma_{23} \\ \Sigma_{13} \\ \Sigma_{12} \end{pmatrix} \quad (2)$$

With the use of the Abaqus plug-in *HomTools*, the macroscopic homogeneous stress $\boldsymbol{\Sigma}$ is automatically computed giving thus a straightforward access to the homogenized stiffness tensor (Figure 1).

3. Convergence Analysis

Kanit *et al.* [2003] proposed a method for determining the typical REV size of a random heterogeneous material at a given precision. This method is based on the integral range theory developed by Lantuejoul [1991], in which the integral range A_3 is a characteristic volume that depends on the microstructure [Lantuejoul, 1991; Kanit *et al.*, 2003]. More precisely, if the two-point correlation function is denoted by

$$C(X, \mathbf{h}) = p\{\mathbf{x} \in X, \mathbf{x} + \mathbf{h} \in X\},$$

the integral range is defined as

$$A_3 = \frac{1}{C(X, 0) - C(X, 0)^2} \int_{R^3} (C(X, \mathbf{h}) - C(X, 0)^2) \, d\mathbf{h} \quad (3)$$

According to Lantuejoul [1991], the variance $D_Z^2(V)$ of a given physical or mechanical property Z decreases as a power law of the ratio between the sample volume V considered and the integral range A_3 of the material. For a porous material of porosity ϕ , this relation reads

$$D_Z^2(V) = \phi(1 - \phi)(Z_m - Z_{\text{air}})^2 \left(\frac{A_3}{V} \right)^{\alpha_Z} \quad (4)$$

where $Z_m - Z_{\text{air}}$ is the property contrast between air and material phases and α_z is an exponent smaller than one that depends both on the property and the boundary value problem considered. The bigger the edge effect, the smaller this exponent.

The relationship (4) implies that estimates of the property Z converge with increasing volume V for a given A_3 . By dividing the sample volume by the integral range of the snow considered, it is possible to restrict the volume convergence analysis of the homogenized mechanical properties of snow to a single arbitrary snow sample and then define a general size for the REV as a multiple (n) of the integral range for any type of snow thanks to equation (4), i.e., $V = n A_3$. In practice, the numerical estimate of the integral range appears to be fairly well approximated by the product of the three correlation lengths (ℓ_1, ℓ_2, ℓ_3) along the axes $\mathbf{e}_1, \mathbf{e}_2$, and \mathbf{e}_3 , which can be computed following the approach proposed in Löwe *et al.* [2013].

In order to evaluate the optimal size of the REV of snow, i.e., the optimal value of n , a volume convergence analysis has been performed on a rounded grain sample of a density of 285 kg m^{-3} and of a typical correlation length $\ell = \sqrt[3]{\ell_1 \ell_2 \ell_3} \propto \sqrt[3]{A_3}$ of $70 \text{ }\mu\text{m}$. Cubic subvolumes of size $V = n A_3 = (m \ell)^3$ were extracted from the raw binary tomographic image, and their homogenized stiffness and compliance matrices were computed following the approach presented in section 2.4.

Figure 1 shows the evolution of the Young's moduli with increasing $(m \ell) = V^{1/3}$ and highlights their convergence toward a constant value. A similar plot was obtained for the shear moduli. As the simulation time increases with V , a compromise between good precision and a reasonable simulation time has to be made. A REV of $(30 \ell)^3$ was chosen to perform all the simulations. Figure 1 also shows that the volume convergence is slower for the Young's moduli of the sample than for its density. This difference in convergence rates is actually formalized by the theoretical expression of the variance given in equation (4) and justifies the approach followed in this paper not to perform the convergence analysis on geometrical properties only.

In parallel, the convergence of the Young's moduli with decreasing mesh size has also been analyzed, using a subvolume with length scale 30ℓ (Figure 1). A very similar plot was obtained for the shear moduli. Again, a compromise between good precision and a reasonable simulation time has to be made. A mesh with 4×10^5 elements, as used in the preceding volume convergence analysis, has been chosen for all simulations.

4. Correlation Between Density and Homogeneous Elastic Properties

The homogeneous elastic properties of a large variety of snow types were computed following the above methodology on 31 images from the 3-D database of the snow research center (CEN) [see, e.g., *Calonne et al.*, 2012]. The numerical data obtained in this study are available in the supporting information linked to this paper.

4.1. Density Influence on the Snow Elastic Properties

Young's moduli, shear moduli, and Poisson's ratio are plotted with respect to the relative density of snow in Figures 2 and 3. Triple "T" shapes are used to show the relative locations of the Young's and shear moduli. The large and small horizontal bars of the triple T lie at the values of the moduli E_1 and E_2 (or G_{23} and G_{13}), and the tip of the vertical bar lies at the value of the modulus E_3 (or G_{12}). For the Poisson's ratio, the average value is plotted together with the interval that contains the six Poisson's ratios presented in (2). Symbol colors correspond to the different types of snow according to the international classification [Fierz *et al.*, 2009].

On a log-log scale, the dependence of the normalized averages of Young's moduli (E_{snow}) and shear moduli (G_{snow}) on density appears to be relatively linear throughout the wide range tested (from 103 to 544 kg m^{-3}). A power law fit gives the first-order dependence relationships with good regression coefficients (R^2):

$$\begin{cases} \frac{E_{\text{snow}}}{E_{\text{ice}}} = 0.78 \left(\frac{\rho_{\text{snow}}}{\rho_{\text{ice}}} \right)^{2.34}, & R^2 = 0.97 \\ \frac{G_{\text{snow}}}{G_{\text{ice}}} = 0.92 \left(\frac{\rho_{\text{snow}}}{\rho_{\text{ice}}} \right)^{2.51}, & R^2 = 0.97 \end{cases}, \quad \text{for } \frac{\rho_{\text{snow}}}{\rho_{\text{ice}}} \in [0.1; 0.6]. \quad (5)$$

The numerical points reported in Figure 2 were compared with the prediction of two energy bounds and two analytical models. The Young's and shear moduli corresponding to the prediction of the classical Voigt bound and the Hashin and Shtrikman upper bound for isotropic material [Hashin and Shtrikman, 1963] were computed for the range of densities considered. The isotropic differential [Zimmerman, 1991] and Mori-Tanaka

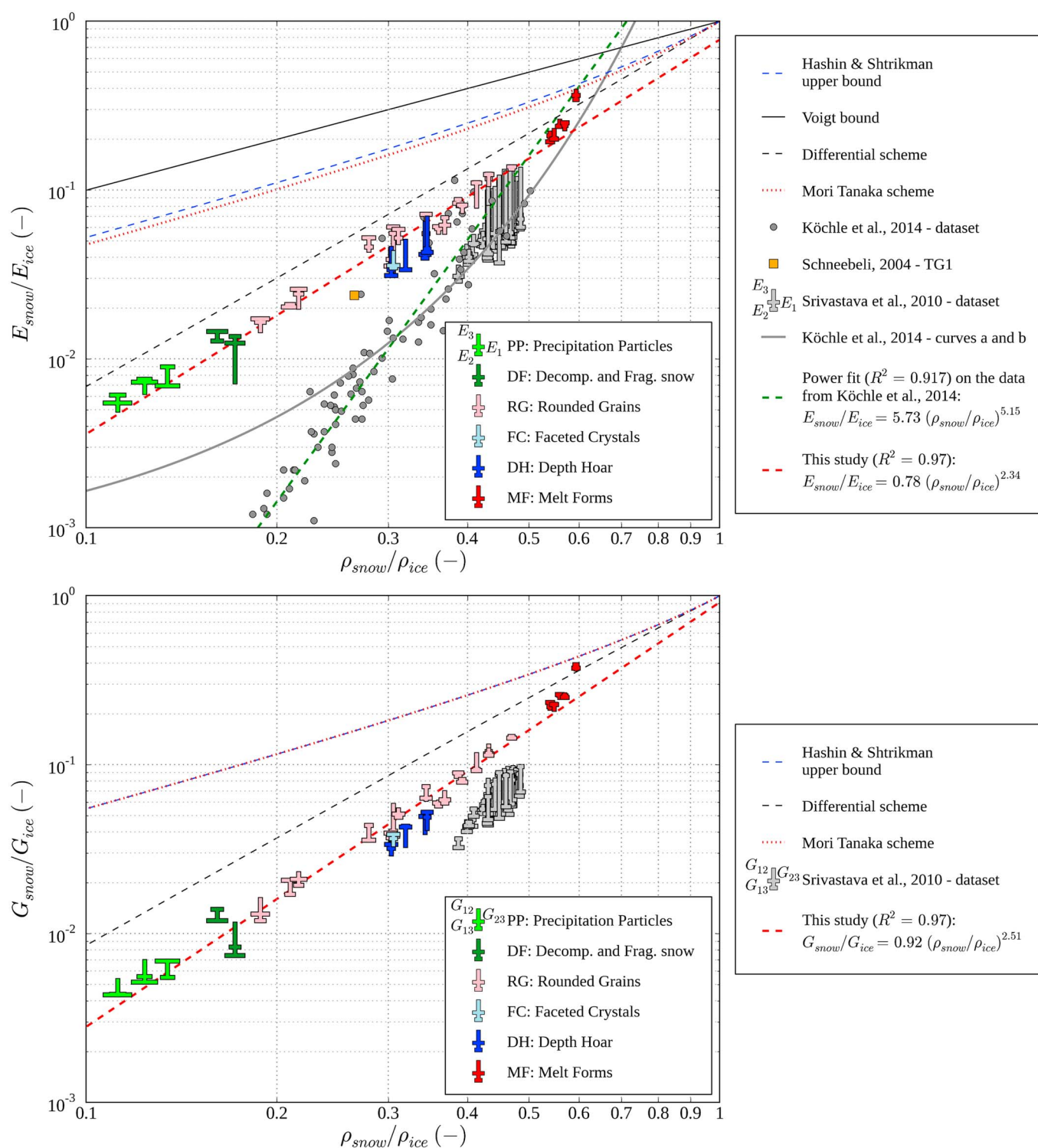


Figure 2. (top) Young's moduli and (bottom) shear moduli dependence with respect to density. Triple T shapes are used in order to distinguish the moduli. Colors correspond to the different snow types [Fierz et al., 2009]. Numerical results of Köchle and Schneebeli [2014], Srivastava et al. [2010], and Schneebeli [2004] are reported, and comparison is made with two energy bounds and two analytical estimates.

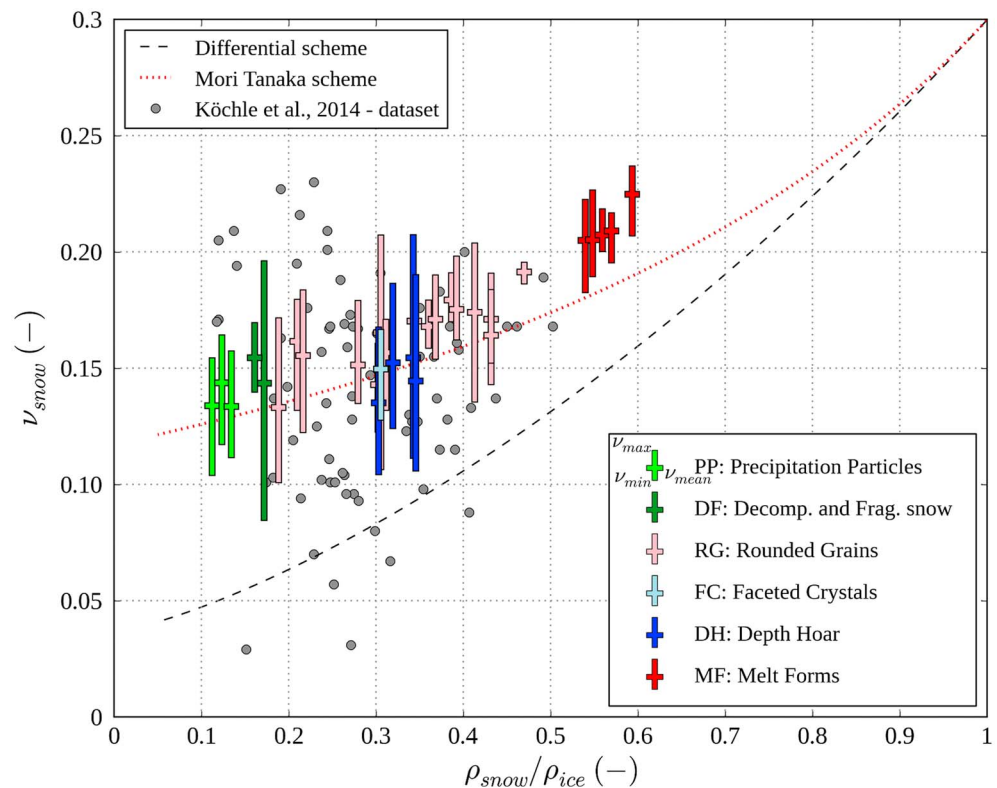


Figure 3. Average Poisson's ratio dependence with respect to density. Vertical bars show the location of the highest and lowest Poisson's ratios. Colors correspond to the different snow types [Fierz *et al.*, 2009]. Comparison is made with two analytical estimates and the data of Köchle and Schneebeli [2014].

[Mori and Tanaka, 1973] schemes for calculating the moduli of materials with inclusions, which can still be used for high-porosity values, were also computed. Finally, in order to evaluate the consistency of our implementation of the KUBC homogenization process to snow, the numerical estimates of the Young's modulus obtained by Köchle and Schneebeli [2014], Srivastava *et al.* [2010], and Schneebeli [2004] are shown in Figure 2. The exponential fit proposed by Köchle and Schneebeli [2014] is plotted in Figure 2, and a power law with a good regression coefficient of $R^2 = 0.917$ is proposed as a better fit to their results:

$$\frac{E_{\text{snow}}}{E_{\text{ice}}} = 5.73 \left(\frac{\rho_{\text{snow}}}{\rho_{\text{ice}}} \right)^{5.15}$$

4.2. Discussion

Figure 2 shows that the proposed power law (5) is a good fit to the point values of the Young's and shear moduli of snow in the whole density range derived from the modeling exercise. It is interesting here to draw a parallel with the analytical models classically used for the elastic properties of cellular materials [Knackstedt *et al.*, 2006; Gibson and Ashby, 1999]. For skeleton cellular materials locally loaded in bending, the relative Young's modulus of the porous material is given by a power law of exponent $n = 2$ of its relative density. However, for membrane cellular materials locally loaded in bending, the relative Young's modulus is given by a power law of exponent $n = 3$ of its relative density. The exponent $n = 2.34$ of the fitted expression (5) is consistent with the predicted behavior of these materials also characterized by a very high porosity. Assuming that the ice grains are also loaded in bending, the macroscopic behavior of snow is closer to a skeleton behavior than that of a membrane.

Both schemes overestimate the values of the Young's moduli, but in contrast to the Mori-Tanaka scheme, the differential scheme gives a relatively good prediction of the exponent of the power law relating normalized Young's modulus and volume fraction of ice. For the shear modulus, the differential scheme is no longer satisfactory. As for Poisson's ratio in Figure 3, the Mori-Tanaka scheme gives a relatively good estimate in contrast to the differential scheme. The two analytical schemes considered were initially developed in order to

model inclusion/matrix materials, and it is not surprising that they cannot account for the connected porosity of snow.

Our results of Figure 2 are the same order of magnitude as those of *Srivastava et al.* [2010] for the density range considered. Similarly, they are consistent with Young's moduli of *Köchle and Schneebeli* [2014] for $\rho_{\text{snow}}/\rho_{\text{ice}} \in [0.4; 0.5]$. However, our results differ significantly from the computations of *Köchle and Schneebeli* [2014] for lower density snow. The major difference between our approach and those found in the literature lies in the boundary conditions used in the homogenization procedure. While we use KUBC boundary conditions, *Köchle and Schneebeli* [2014] simulated a uniaxial compression test which requires a much bigger REV size. In addition, to deduce the Young's modulus value from numerical simulations, *Köchle and Schneebeli* [2014] were forced to postulate a macroscopic isotropic behavior for all their samples. Furthermore, the voxel size of the images used by *Köchle and Schneebeli* [2014] is 3 to 7 times bigger than the one used in our study. These differences in the testing procedure might result in the observed differences in Figure 2.

The last comment to be made on the results shown in Figures 2 and 3 is that many samples present an anisotropic behavior that cannot be captured by the density parametrizations of the macroscopic properties of snow given in (5). The degree of anisotropy of a given type of snow can be estimated using two indicators $A(E)$ and $A(G)$ defined as

$$A(E) = \frac{E_3}{(E_1 + E_2)/2} \quad \text{and} \quad A(G) = \frac{G_{12}}{(G_{23} + G_{13})/2} \quad (6)$$

where E_3 and G_{12} are the Young's and shear moduli linked to the vertical direction. A perfectly isotropic material would exhibit anisotropy indicators equal to 1. For all the samples considered, we have $A(E) \in [0.56; 1.57]$ and $A(G) \in [0.77; 1.47]$ with a significant influence of the snow type.

5. Influence of the Type of Metamorphism on the Mechanical Properties

Even when occurring at constant density, the metamorphism of snow strongly influences its macroscopic behavior [*Schneebeli*, 2004; *Srivastava et al.*, 2010; *Calonne et al.*, 2014a]. In this section, three types of snow metamorphism are considered in order to assess their influence on the mechanical properties of snow. For each of them, the time evolution of density, Young's moduli (E_1, E_2, E_3), and shear moduli (G_1, G_2, G_3) are plotted in Figure 4.

5.1. Isothermal Experiment

The first temporal series considered consists of eight microtomographic images taken from *Flin et al.* [2004]. Fifteen hours after a snowfall, a natural snow layer was placed in isothermal conditions and the metamorphism of the snow microstructure was monitored over 3 months. Samples were regularly extracted from the middle of the layer, impregnated with 1-chloronaphtalene and stored at -20°C . They were then imaged by microtomography.

Snow density increases (Figure 4) due to the settling of snow under its own weight. The Young's and the shear moduli follow this increase. Because of the relatively small thickness of the snow layer considered (about 10 cm), no huge anisotropy appears with respect to the privileged direction of compaction \mathbf{e}_3 . During the whole experiment, the anisotropy indicators remain relatively constant with $A(E) \in [0.85; 1.03]$ and $A(G) \in [0.95; 1.28]$. However, as it has been observed by *Flin et al.* [2004], the snow grains tend to rearrange with their longest dimension along the horizontal direction. This might be related to the fact that the vertical Young's modulus is systematically the lowest one after 600 h. Overall, isothermal metamorphism resulted in a noticeable densification of the snow sample and, thus, in an increase in its stiffness. This observation is consistent with the practical knowledge that the mechanical stability of a snowpack increases with time after a snowfall, provided that no temperature gradient (TG) metamorphism occurs.

5.2. Temperature Gradient Experiment

The second temporal series consists of the seven microtomographic images of *Calonne et al.* [2014a]. They were obtained during a TG experiment at -4°C . A temperature gradient of 43 K m^{-1} was applied to a sieved snow layer for 500 h, and samples were regularly extracted from the middle of the layer and imaged by microtomography.

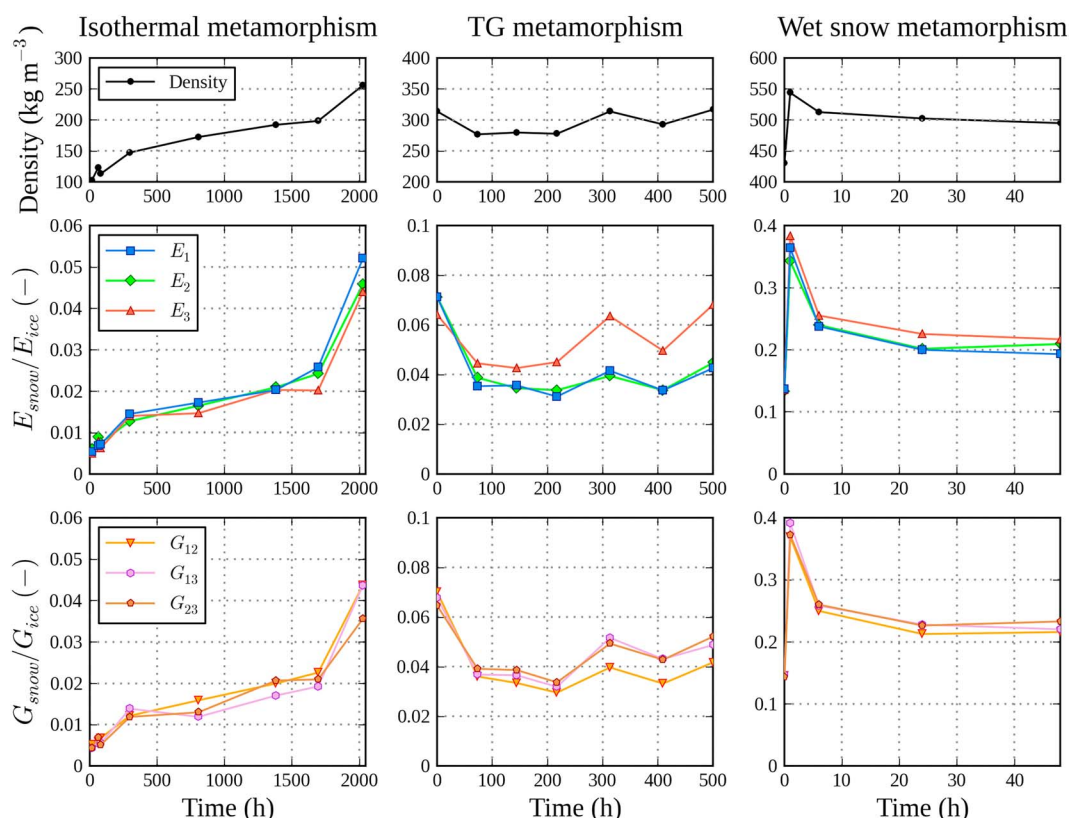


Figure 4. Time evolution of (middle row) the three Young's moduli and (bottom row) the three shear moduli of snow during three temporal experiments. (top row) The time evolution of the snow density is also represented.

In the corresponding plot of Figure 4, it can be seen that the general fluctuations of the relative moduli follow the small fluctuations in density observed between the different images. In addition, development of an anisotropic mechanical behavior can be seen with the appearance of an increasing gap between the vertical (E_3) and horizontal (E_1 ; E_2) Young's moduli and between the shear modulus G_{12} and the other shear moduli. The anisotropy indicators $A(E)$ and $A(G)$ defined in (6) vary from 0.89 to 1.08, respectively, at the beginning of the experiment to 1.56 and 0.83 at the end.

The fast initial decrease in the values of the Young's moduli might be related to the initial reorganization of the small ice bridges between grains [Calonne *et al.*, 2014a]. Because of the vertical orientation of the water vapor fluxes, horizontal bridges are more likely to disappear than the vertical ones. This may explain the lower initial decrease of the vertical Young's modulus E_3 . With the elongation of the microstructure in the vertical direction, more ice is involved in vertical compression or shear solicitations than in their horizontal counterparts. This microstructure evolution is thus consistent with the relative increase in the vertical Young's modulus E_3 and the shear moduli G_{13} and G_{23} and with the results of Calonne *et al.* [2014a] concerning the physical and geometrical properties of snow (thermal conductivity, Gaussian curvature, etc.). Overall, most of the moduli decrease from the initial to the final state, which is consistent with the well-known fact that TG metamorphism is a cause of weak snow layer formation.

5.3. Wet Snow Metamorphism Experiment

The third temporal series consists of five microtomographic images taken from Flin *et al.* [2011]. They were obtained during a grain coarsening experiment. Snow porosity was saturated with water kept at 0°C, and the coarsening of this wet snow was monitored over 142 h by sampling several specimens and imaging them by microtomography.

The first increase in density is related to residual liquid water that remained in the sample due to capillary forces and froze before the sample was completely dried. After this, the Young's and shear moduli remain nearly constant and evolve in an isotropic way ($A(E) \in [1.00; 1.12]$ and $A(G) \in [0.94; 1.00]$). This is quite puzzling because the microstructure changed noticeably during the experiment. However, the lack of change

in the mechanical properties can be explained by the fact that while the ice bridges between ice grains are growing, their number per volume unit is decreasing. Overall, wet snow metamorphism seems to have little impact on snow mechanical properties provided that liquid water has been drained before refreezing. Otherwise, the increase in density due to refreezing would significantly strengthen the structure, which is consistent with practical experience of the effect of melt freeze on the mechanical properties of snow.

6. Conclusion and Outlooks

In this work, a numerical homogenization method that can capture the full 3-D macroscopic mechanical behavior of snow was successfully developed. A rigorous use of the theoretical results of the homogenization theory was made in the definition of the boundary value problem to be solved on the REV. The optimal REV size, estimated by a convergence analysis of the computed effective properties, and not merely as a function of density, can be expressed in terms of correlation lengths.

Thanks to this powerful numerical procedure, the effective elastic properties of snow have been computed for a wide range of densities and snow types. We have found that for our samples, the homogenized elastic stiffness tensor is mainly orthotropic. Simple power laws, valid over the whole range of densities tested, have been proposed to link the Young's and shear moduli of snow to its density, and the degree of anisotropy of these properties has been quantified.

The influence of the three main types of metamorphism on the effective elastic properties of snow has been also investigated. The numerical results obtained are in good agreement with the qualitative effects induced by each metamorphism type on the mechanical properties of snow.

Among several applications, these results have potential impacts on avalanche risk forecasting. In particular, the regression equation (5) can be applied to existing snowpack models such as Crocus [Brun *et al.*, 1992] or SNOWPACK [Bartelt and Lehning, 2002] to estimate the elastic properties of each layer, which is of particular interest for weak layers [Köchle and Schneebeli, 2014] and the fracture models of slab avalanche release [see, e.g., Schweizer and Camponovo, 2002; Heierli *et al.*, 2008; Gaume *et al.*, 2015].

The proposed methodology might easily be transposed to the study of other materials, provided that the 3-D images of their microstructure are available and that the constitutive behavior of their constituents is known. Our numerical procedure can also be applied to investigate more complex behavior of snow such as its 3-D viscoplastic behavior, which plays a part in the snowpack densification process. Such a work is currently in progress and may help improve the long-term evolution of the snowpack in forecasting models.

Acknowledgments

We thank S. Lejeunes and S. Bourgeois from the LMA for sharing with us the code of their plug-in HOMTOOLS and for their help to use it in our scripts. We also thank P. K. Srivastava for providing the numerical data of his previous study [Srivastava *et al.*, 2010]. Results of Köchle and Schneebeli [2014] were downloaded from their supplementary material: <http://www.igsoc.org/hyperlink/13j220suppl.pdf>. Tomographic images have been acquired at ESRF (ID19) and 3SR Lab. CNRM-GAME/CEN is part of the LabEx OSUG@2020 (ANR-10-LABX-0056), and 3SR Lab is part of the LabEx Tec 21 (ANR-11-LABX-0030).

The Editor thanks Ian Baker and an anonymous reviewer for their assistance in evaluating this paper.

References

- Adams, E. E., and D. J. Walters (2014), Fine structure layering in radiation recrystallized snow, *International Snow Science Workshop 2014 Proceedings, Banff, Canada*, pp. 29–34.
- Auriault, J.-L., C. Boutin, and C. Geindreau (2010), *Homogenization of Coupled Phenomena in Heterogeneous Media*, vol. 149, John Wiley, London.
- Bartelt, P., and M. Lehning (2002), A physical SNOWPACK model for the Swiss avalanche warning: Part I—Numerical model, *Cold Reg. Sci. Technol.*, 35(3), 123–145.
- Brun, E., P. David, M. Sudul, and G. Brunot (1992), A numerical model to simulate snow-cover stratigraphy for operational avalanche forecasting, *J. Glaciol.*, 38(128), 13–22.
- Brzoska, J.-B., C. Coléou, B. Lesaffre, S. Borel, O. Brissaud, W. Ludwig, E. Boller, and J. Baruchel (1999), 3D visualization of snow samples by microtomography at low temperature, *ESRF Newsletter*, 32, 22–23.
- Calonne, N., F. Flin, S. Morin, B. Lesaffre, S. R. du Roscoat, and C. Geindreau (2011), Numerical and experimental investigations of the effective thermal conductivity of snow, *Geophys. Res. Lett.*, 38, L23501, doi:10.1029/2011GL049234.
- Calonne, N., C. Geindreau, F. Flin, S. Morin, B. Lesaffre, S. Rolland du Roscoat, and P. Charrier (2012), 3-D image-based numerical computations of snow permeability: Links to specific surface area, density, and microstructural anisotropy, *The Cryosphere*, 6(5), 939–951, doi:10.5194/tc-6-939-2012.
- Calonne, N., F. Flin, C. Geindreau, B. Lesaffre, and S. Rolland du Roscoat (2014a), Study of a temperature gradient metamorphism of snow from 3-D images: Time evolution of microstructures, physical properties and their associated anisotropy, *The Cryosphere*, 8(6), 2255–2274, doi:10.5194/tc-8-2255-2014.
- Calonne, N., C. Geindreau, and F. Flin (2014b), Macroscopic modeling for heat and water vapor transfer in dry snow by homogenization, *J. Phys. Chem. B*, 118(47), 13,393–13,403, doi:10.1021/jp5052535.
- Calonne, N., *et al.* (2015), CellDyM: A room temperature operating cryogenic cell for the dynamic monitoring of snow metamorphism by time-lapse X-ray microtomography, *Geophys. Res. Lett.*, 42, 3911–3918, doi:10.1002/2015GL063541.
- Chandel, C., P. K. Srivastava, and P. Mahajan (2014), Micromechanical analysis of deformation of snow using X-ray tomography, *Cold Reg. Sci. Technol.*, 101, 14–23.
- Chen, S., and I. Baker (2010), Evolution of individual snowflakes during metamorphism, *J. Geophys. Res.*, 115, D21114, doi:10.1029/2010JD014132.

- Dormieux, L., and E. Bourgeois (2002), *Introduction à la Micromécanique Des Milieux Poreux*, Presses de l'École nationale des ponts et chaussées, Paris.
- Fang, Q., and D. A. Boas (2009), Tetrahedral mesh generation from volumetric binary and grayscale images, in *IEEE International Symposium on Biomedical Imaging: From Nano to Macro, 2009. ISBI'09*, pp. 1142–1145, IEEE, Boston, Mass.
- Fierz, C., R. L. Armstrong, Y. Durand, P. Etchevers, E. Greene, D. M. McClung, K. Nishimura, P. K. Satyawali, and S. A. Sokratov (2009), *The International Classification for Seasonal Snow on the Ground*, UNESCO/IHP, Paris.
- Flin, F., and J.-B. Brzoska (2008), The temperature-gradient metamorphism of snow: Vapour diffusion model and application to tomographic images, *Ann. Glaciol.*, 49(1), 17–21.
- Flin, F., J.-B. Brzoska, B. Lesaffre, C. Coléou, and R. A. Pieritz (2004), Three-dimensional geometric measurements of snow microstructural evolution under isothermal conditions, *Ann. Glaciol.*, 38(1), 39–44.
- Flin, F., B. Lesaffre, A. Dufour, L. Gillibert, A. Hasan, S. Rolland du Roscoat, S. Cabanes, and P. Pugliese (2011), On the computations of specific surface area and specific grain contact area from snow 3D images, in *Physics and Chemistry of Ice*, edited by Y. Furukawa, pp. 321–328, Hokkaido Univ. Press, Sapporo, Japan.
- Gaume, J., G. Chambon, N. Eckert, M. Naaim, and J. Schweizer (2015), Influence of weak layer heterogeneity and slab properties on slab tensile failure propensity and avalanche release area, *The Cryosphere*, 9(2), 795–804, doi:10.5194/tc-9-795-2015.
- Gibson, L. J., and M. F. Ashby (1999), *Cellular Solids: Structure and Properties*, Cambridge Univ. Press, Cambridge.
- Hagenmuller, P., T. C. Theile, and M. Schneebeli (2014), Numerical simulation of microstructural damage and tensile strength of snow, *Geophys. Res. Lett.*, 41, 86–89, doi:10.1002/2013GL058078.
- Hashin, Z., and S. Shtrikman (1963), A variational approach to the theory of the elastic behaviour of multiphase materials, *J. Mech. Phys. Solids*, 11(2), 127–140.
- Heierli, J., P. Gumbsch, and M. Zaiser (2008), Anticrack nucleation as triggering mechanism for snow slab avalanches, *Science*, 321(5886), 240–243.
- Hill, R. (1963), Elastic properties of reinforced solids: Some theoretical principles, *J. Mech. Phys. Solids*, 11, 357–372.
- Kämpfer, T., M. Schneebeli, and S. Sokratov (2005), A microstructural approach to model heat transfer in snow, *Geophys. Res. Lett.*, 32, L21503, doi:10.1029/2005GL023873.
- Kanit, T., S. Forest, I. Galliet, V. Mounoury, and D. Jeulin (2003), Determination of the size of the representative volume element for random composites: Statistical and numerical approach, *Int. J. Solids Struct.*, 40(13), 3647–3679.
- Knackstedt, M. A., C. H. Arns, M. Saadatfar, T. J. Senden, A. Limaye, A. Sakellariou, A. P. Sheppard, R. M. Sok, W. Schrof, and H. Steininger (2006), Elastic and transport properties of cellular solids derived from three-dimensional tomographic images, *Proc. R. Soc. London, Ser. A*, 462(2073), 2833–2862.
- Köchle, B., and M. Schneebeli (2014), Three-dimensional microstructure and numerical calculation of elastic properties of alpine snow with a focus on weak layers, *J. Glaciol.*, 60(222), 705–713.
- Lantuejoul, C. (1991), Ergodicity and integral range, *J. Microsc.*, 161(3), 387–403.
- Lejeunes, S., et al. (2011), Une toolbox abaqus pour le calcul de propriétés effectives de milieux hétérogènes. in: 10e colloque national en calcul des structures.
- Löwe, H., F. Riche, and M. Schneebeli (2013), A general treatment of snow microstructure exemplified by an improved relation for thermal conductivity, *The Cryosphere*, 7(5), 1473–1480, doi:10.5194/tc-7-1473-2013.
- Mellor, M. (1975), A review of basic snow mechanics, in *Proceedings of the Grindelwald Symposium, 1974, Snow Mechanics*, vol. 114, pp. 251–291, IAHS publication, Grindelwald, Switzerland.
- Mori, T., and K. Tanaka (1973), Average stress in matrix and average elastic energy of materials with misfitting inclusions, *Acta Metall.*, 21(5), 571–574.
- Pieritz, R. A., J.-B. Brzoska, F. Flin, B. Lesaffre, and C. Coléou (2004), From snow X-ray microtomograph raw volume data to micromechanics modeling: First results, *Ann. Glaciol.*, 38, 52–58, doi:10.3189/172756404781815176.
- Pinzer, B., M. Schneebeli, and T. Kämpfer (2012), Vapor flux and recrystallization during dry snow metamorphism under a steady temperature gradient as observed by time-lapse micro-tomography, *Cryosphere*, 6, 1141–1155.
- Schleef, S., H. Löwe, and M. Schneebeli (2014), Hot-pressure sintering of low-density snow analyzed by X-ray microtomography and in situ microcompression, *Acta Mater.*, 71, 185–194.
- Schneebeli, M. (2004), Numerical simulation of elastic stress in the microstructure of snow, *Ann. Glaciol.*, 38(1), 339–342.
- Schulson, E. M., and P. Duval (2009), *Creep and Fracture of Ice*, Cambridge Univ. Press, Cambridge, U. K.
- Schweizer, J., and C. Camponovo (2002), The temperature dependence of the effective elastic shear modulus of snow, *Cold Reg. Sci. Technol.*, 35(1), 55–64, doi:10.1016/S0165-232X(02)00030-7.
- Shapiro, L. H., J. B. Johnson, M. Sturm, and G. L. Blaisdell (1997), *Snow Mechanics: Review of the State of Knowledge and Applications*, U. S. Army Cold Reg. Res. and Eng. Lab., Springfield, Va.
- Srivastava, P., P. Mahajan, P. Satyawali, and V. Kumar (2010), Observation of temperature gradient metamorphism in snow by X-ray computed microtomography: Measurement of microstructure parameters and simulation of linear elastic properties, *Ann. Glaciol.*, 51(54), 73–82.
- Van Rietbergen, B., A. Odgaard, J. Kabel, and R. Huiskes (1996), Direct mechanics assessment of elastic symmetries and properties of trabecular bone architecture, *J. Biomech.*, 29(12), 1653–1657.
- Zimmerman, R. W. (1991), Elastic moduli of a solid containing spherical inclusions, *Mech. Mater.*, 12(1), 17–24.